Journal of Materials Chemistry A

PAPER

View Article Online
View Journal | View Issue

Cite this: J. Mater. Chem. A, 2016, 4, 15621

Investigation of a microporous iron(III) porphyrin framework derived cathode catalyst in PEM fuel cells†

N. M. Cantillo,*[a] G. A. Goenaga,[a] W. Gao,[b] K. Williams,[b] C. A. Neal,[a] S. Ma,[b] K. L. More[c] and T. A. Zawodzinski, Jr.*[ac]

Received 13th April 2016
Accepted 15th September 2016

DOI: 10.1039/c6ta03059a

www.rsc.org/MaterialsA

In Polymer Electrolyte Membrane Fuel Cells (PEMFCs) the thickness, structure and morphology of the electrode layer play an important role in the cell performance. This effect becomes particularly significant when the cathode catalyst is based on a non-precious metal due to the higher catalyst loadings required to compensate for the lower catalytic activity when compared to Pt based catalysts. In this study, an iron(III) porphyrin framework material was synthesized and pyrolyzed and its catalytic activity towards the oxygen reduction reaction (ORR) was evaluated using rotating disk electrode (RDE) experiments and single cell testing. Single cell performance was evaluated as a function of the electrode catalyst loading (electrode thickness) and oxygen partial pressure. As expected, the ORR kinetic overpotential was the major contributor to the overall voltage loss. However, the mass transport contribution to the voltage loss became more prominent with small increases in the cathode catalyst loading. The observed performance is discussed in the context of structure and morphology of the catalyst layer (CL), analyzed through scanning electron microscopy (SEM), transmission electron microscopy (TEM), and X-ray diffraction (XRD).

Introduction

The sluggish ORR accounts for most of the voltage loss in PEMFCS, even when the best Pt-based catalysts are employed.[1] This factor, in addition to the low availability and high cost of Pt, has motivated the search for non-precious metal catalysts (NPMCs) in order to decrease the cost and facilitate the commercialization of PEMFCs.

Among the evaluated NPMC alternatives, those derived from heat-treated metal/nitrogen/carbon have produced the best results in terms of ORR activity.[2–7] Although early studies mainly focused on materials obtained from transition-metal-based macrocycles,[8,9] preparation of catalysts from pyrolyzed separate metal, nitrogen, and carbon precursors has been widely explored since 1989.[10] This approach offers a great variety of possibilities in terms of precursors and synthesis conditions. The precedent for this method was set by Yeager *et al.*,[10] who reported the use of poly(acrylonitrile) (PAN) and a metal precursor (cobalt or iron) loaded onto a carbon support and pyrolyzed at 800 °C in argon. The materials obtained exhibited ORR activity comparable to that of heat-treated cobalt porphyrins.

Yeager's work[10] motivated the subsequent study of many other nitrogen containing compounds, including N-containing polymers as dual carbon and nitrogen precursors, which can facilitate the formation of nitrogen containing sites on the graphitic carbon surface during the catalyst synthesis.[11] Studies involving PAN plus metal[12–14] have been reported, emphasizing the importance of the simultaneous presence of the metal salt and the nitrogen precursor during the heat treatment process.[12] Some of this work explored PAN-based nanostructured materials, such as aerogel composites,[13] N-doped ordered porous carbons,[14] and carbon-nitride (CN_x)/PAN nanofibers[15] as catalyst precursors. Substantial ORR activities were reported. Lalande *et al.*,[16] in turn, explored the importance of different atoms (N, metal or both) in the generation of the catalytic site by employing polyvinylferrocene as a nitrogen-free precursor. The material obtained through a single-step pyrolysis did not exhibit any catalytic activity for the ORR. However, it was possible to obtain an active catalyst through a second pyrolysis step in the presence of a nitrogen source such as acetonitrile vapor.

Heterocyclic polymers, particularly pyrrole derivatives, have also been widely studied as nitrogen-containing precursors since 1990.[14,17–24] This provides the possibility to mimic the atomic configuration of metal-containing porphyrins. It is assumed that the metal atom bonds to pyrrole units, allowing the formation of Me–N sites upon pyrolysis.[20] Major progress in

[a]Chemical and Biomolecular Engineering Department, University of Tennessee, Knoxville, TN, USA. E-mail: ncantill@vols.utk.edu

[b]Department of Chemistry, University of South Florida, Tampa, FL, USA

[c]Oak Ridge National Laboratory, Oak Ridge, USA

† Electronic supplementary information (ESI) available. See DOI: 10.1039/c6ta03059a

achieving fuel cell-relevant performance through this approach was reported with the publication from Wood *et al.*[25] In this case, nitroaniline was mixed with an anhydrous metal salt (generally an iron chloride) and polymerized in the presence of carbon, activated by firing in the presence of ammonia, and ball-milled and subjected to an optional second firing, which proved to be beneficial in terms of catalytic activity. Finally, the milled catalyst was acid washed to remove the leachable portion of transition metals. The material showed high ORR onset voltages, above 0.9 V, and a volumetric current density of 19 A cm^{-3} at 0.8 V.

Significant improvement was achieved with NPMCs prepared using heterocyclic polymers such as polyaniline (PANI)[2,11,26–29] as precursors. Zelenay's group reported a comparison of PANI and polypyrrole (PPy) as nitrogen precursors for iron based catalyst synthesis,[26] obtaining better performance with respect to stability and selectivity with the former. Promising durability results were obtained with PANI–FeCo–C catalysts (700 hour-fuel cell performance test at a constant cell voltage of 0.4 V). These materials were synthesized by mixing a short-chain aniline oligomer with high-surface area carbon material, and transition metal precursors, followed by the addition of an oxidant to polymerize the aniline. After polymerization, water was removed and the sample was subjected to a 900 °C heat treatment under a N_2 atmosphere, leached in H_2SO_4 for 8 hours and subsequently subjected to a second heat treatment. High power density (0.38 W cm^{-2} at 0.6 V) was reached in fuel cell operation (H_2–O_2)[2] with these materials. PANI-based nanostructured materials have also been studied with promising results.[15,28]

Advances have also been made through the enhancement of the mass-transport properties of the catalyst material.[6,14,29–33] In particular, metal–organic frameworks (MOFs) have been employed due to the accessibility of metal cation in their structure, high volumetric density of metal-ion sites and high micropore surface area.[34,35] Liu and co-workers[30,31] were the first to implement this approach, selecting a cobalt-based zeolitic imidazolate framework (ZIF, a subclass of MOFs with imidazolate as ligand) as a precursor for the synthesis of ORR catalysts through pyrolysis. Maximum performance, with an onset potential of 0.83 V, was achieved after pyrolysis at a temperature of 750 °C, comparable to the best cobalt-based NPMCs.[36] In 2011, Dodelet's group selected a Zn-based ZIF, covered with a small amount of iron–phenanthroline complex as catalyst precursor.[7] A power density of 0.91 W cm^{-2} at 0.6 V (H_2/O_2, 1 bar gauge pressure, 4 mg cm^{-2}), comparable to that of a state-of-the-art platinum-based cathode having a loading of 0.3 mg_{Pt} cm^{-2}, was reported with this material. However, the stability tests showed a significant decay in current density over 100 h of operation. Recent studies with this material have involved the use of an iron porphyrin (as iron and nitrogen precursor), in order to study the effect of the pyrolysis temperature on the resulting stability.[35]

As an additional approach, amorphous porous organic polymers (POPs), have been extensively studied over the last decade.[37–41] Catalysts derived from these precursors exhibit exceptional characteristics in terms of surface area, uniform pore sizes, and stability. Recently, Ma *et al.* reported the construction of a porphyrin-based conjugated porous organic polymer, named CHF-1 (CHF denotes covalent heme framework), utilizing a custom-designed porphyrin complex, iron(III) *meso*-5,10,15,20-tetrakis (4-bromophenyl)porphyrin chloride (Fe(tbpp)Cl), as a building block.[41] This material was designed as a biomimetic oxidation catalyst,[41] but its potential as an ORR catalyst is investigated in this work.

To summarize the discussion above, important advances have been achieved with NPMCs in terms of catalytic activity and durability. However, to date only Olson *et al.*[42] have reported a detailed study of the effect on performance of parameters such as CL thickness and composition in electrodes in fuel cells. Through a ΔE *vs.* i analysis on a cobalt-based cathode catalyst, they found that transport limitations were appreciable even at relatively low current density. The non-platinum CL in Olson's study includes the addition of PTFE-supported carbon (PTFE/C) composite powder.[42]

In the present contribution, we study the ORR activity of the CHF-1 catalyst described above after pyrolysis at 700 °C under inert atmosphere. RDE and RRDE experiments are performed to determine the onset potential and number of electrons transferred. The structure and properties of the material are characterized using transmission electron microscopy (TEM), scanning electron microscopy (SEM), X-ray diffraction (XRD) and surface area analysis. Furthermore, this paper proposes a methodology for non-precious metal catalyst evaluation in low temperature fuel cells under realistic operation conditions and proposes a methodology for non-precious metal catalyst evaluation, and identification of the individual voltage loss contributions.

Experimental

Catalyst synthesis and activation

The CHF-1 was prepared according to the procedure described previously.[41] Briefly, iron(III) tetra (4-bromophenyl)porphyrin chloride was added to a solution of 2,2′-bipyridyl, bis(1,5-cyclooctadiene)-nickel(0) and 1,5-cyclooctadiene in anhydrous DMF/1,4-dioxide. This mixture was stirred at room temperature under argon atmosphere overnight, and subsequently cooled in an ice bath. Finally, a 50% acetic acid solution was added and the resulting mixture was stirred for another night and then washed and dried in vacuum to give CHF-1 in 78% yield.

The as-synthesized materials exhibit very low ORR catalytic activity as determined by the RDE experiment (Fig. 1A). The prepared catalyst was thermally activated under inert atmosphere (N_2 gas) at 700 °C for 1 hour, based on previous experiments carried out in our laboratory (Fig. S1†). This was followed by acid treatment in 0.5 M H_2SO_4 at 80 °C for 8 hours, with the purpose of removing metal generated during pyrolysis.[43] Then the sample is subjected to a second heat treatment at 700 °C for 1 hour in an inert atmosphere to promote the formation of additional catalytic centers.[11]

Physicochemical characterization

The surface area and the pore size and volume of the catalysts were measured with a Quantachrome Instruments Autosorb iQ

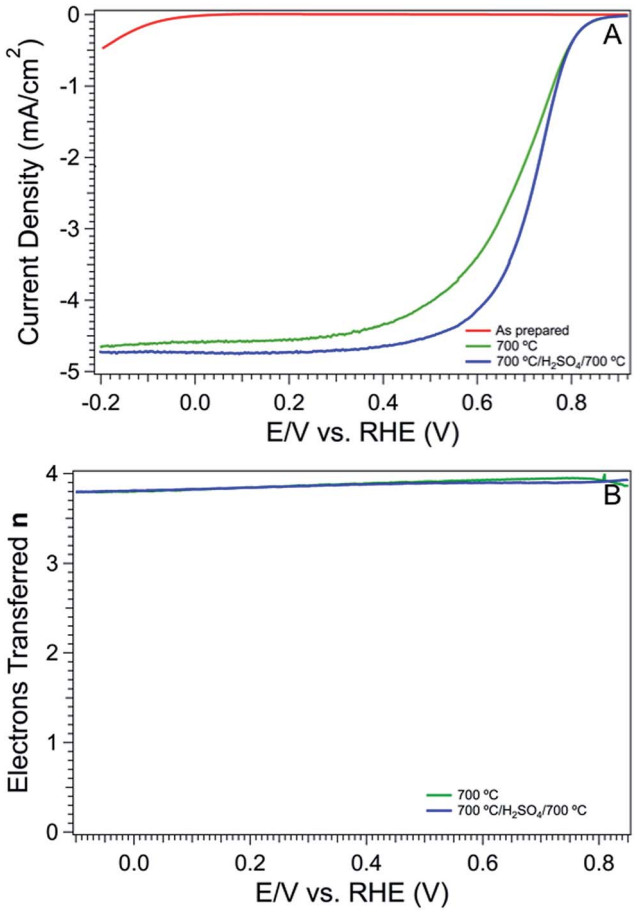

Fig. 1 RDE curves (A) for the as-prepared and pre-treated iron porphyrin framework (1600 rpm, 10 mV s^{-1} scan rate. 0.1 M H_2SO_4 electrolyte, Hg/Hg_2SO_4 reference electrode and Au wire counter electrode) and number of electrons transferred (B) for the pre-treated iron porphyrin framework catalyst (ring electrode is kept at 1.2 V).

with nitrogen as the adsorbate. Brunauer–Emmett–Teller (BET) and Barrett–Joyner–Halenda (BJH) Pore Size ND Volume Analysis was employed for to analyze this data. The quantification of the metal was performed using Inductively Coupled Plasma/Optical Emission Spectrometry (ICP-OES).

XRD, SEM and TEM were used to characterize the materials. XRD patterns were measured with a Bruker D2 Phaser diffractometer with Cu Kα radiation. For SEM imaging, a Hitachi S-4800 field emission scanning electron microscope was employed; this equipment features a resolution of 1.0 nm and a variable acceleration voltage of 0.5–30 kV. A 300 kV HF-3300 TEM/STEM, with a cold-field emission gun and 0.13 nm resolution was used to analyze the microstructure of the materials.

Rotating ring disk electrode (RRDE) experiments

Inks were prepared by mixing 5 mg of the catalysts with 5 wt% Nafion® solution (Sigma-Aldrich) in a 30/70 ionomer to catalyst ratio, with methanol as the solvent. Inks were stirred for at least one day and sonicated for 10 minutes before preparing the electrodes. 15 μl of the ink was deposited on a glassy carbon (GC) electrode disk to achieve loadings of 600 μg cm^{-2}. A typical three-electrode cell system with a gold wire counter electrode and Hg/Hg_2SO_4 reference electrode saturated with 0.5 M H_2SO_4 was used. The potential of the reference electrode *vs.* the reversible hydrogen electrode (RHE) was measured experimentally by saturating the electrolyte with hydrogen for at least 30 minutes and measuring the open circuit potential using a Pt working electrode. The potential was determined to be 0.696 V *vs.* RHE. All potentials are reported *vs.* RHE.

The working electrode consisted of a GC disk with a Pt ring (AFE7R9GCPT from Pine Instruments) with a collection efficiency of 37%. The electrode potential was controlled using a multi-channel VSP3 potentiostat from BioLogic Science Instruments. The rotation speed of the working electrode was controlled with an AFMSRCE Pine Modulated Speed Rotator (MSR) and held constant at 1600 rpm. The experiments were conducted in a 0.1 M H_2SO_4 solution at room temperature. Voltammograms were collected at 10 mV s^{-1} scan rate, static and rotating, with the electrolyte saturated with nitrogen, for background correction, and oxygen. Before each experiment, the GC disk was mechanically polished with 5 μm and 0.05 μm size alumina powder.

RDE experiments were performed in solutions of electrolyte saturated with oxygen at different oxygen partial pressures. For this purpose, oxygen and argon were mixed using two high precision Cole–Parmer multi-gas MC series mass flow controllers. The partial pressure of oxygen was varied from 5 to 100%.

Membrane electrode assembly preparation

To prepare electrodes for the FC experiments, cathode catalyst inks were prepared by ultrasonically mixing 15 mg of the pyrolyzed/acid treated catalyst powder with 1 ml of deionized water, 2 ml of isopropanol and 175 mg of 5 wt% Nafion® solution. The ink was sprayed onto a 5 cm^2 gas diffusion layer (GDL) using an airbrush, until the desired catalyst loading was reached (1 mg_{cat} cm^{-2}, 2 mg_{cat} cm^{-2} and 3 mg_{cat} cm^{-2}). The cathode CL thickness was measured for each loading, using an Absolute Mitutoyo® Digimatic Indicator (Model ID-S112PE).

GDLs made of carbon paper with a carbon coating (SIGRACET® Gas Diffusion Media, Type GDL 25 BC) were used for both electrodes. The Nafion® content in the dry cathode was 30 wt%, which corresponds to the ratio that provided the best results in a previous study performed in our laboratory (Fig. S3†). The anode electrodes, on the other hand, were prepared by hand painting. The anode ink was prepared from BASF 30% platinum on Vulcan XC-72. Anode loadings were 0.3 mg_{Pt} cm^{-2} with a 2 : 1 ionomer : Pt ratio. The cathode and anode electrodes were hot-pressed against either side of a 212 Nafion® membrane at 140 °C for 10 minutes using a load of 1000 kg.

Fuel cell testing

Single cell experiments on the prepared MEAs were performed using a Fuel Cell Technologies test stand and single cell hardware. A BioLogic VSP3 potentiostat with a 10 A booster was used to collect polarization curves and electrochemical impedance spectroscopy (EIS) data. The cell has a serpentine flow channel

and an active area of 5 cm^2. The temperature for all experiments was 80 °C, backpressure at both electrodes was 29.4 bar psia, and all gases were at 100% relative humidity (RH). The flow rate of ultra-high purity (UHP) H_2 at the anode was held constant at 0.1 L min^{-1} and UHP O_2 flow was kept at 0.2 L min^{-1}.

The testing protocol was the following: the cell was held at open circuit voltage (OCV) for 10 minutes; then the voltage was held at 0.6 V for 15 min, followed by 0.4 V for 10 min for conditioning. A polarization curve was obtained by changing the potential from OCV to 0.2 V, decreasing the potential in steps of 2 mV from OCV to 0.65 and 20 mV from 0.65 V to 0.2 V, each potential was held constant for 30 seconds before recording the current. Measurements were performed with different oxygen partial pressures in the cathode feed, ranging from 20 to 100%, obtained by mixing oxygen and argon gases, as described above. All overpotentials are reported using the reversible OCV as reference.

To evaluate the behavior of our catalyst in an actual fuel cell, we need to disentangle kinetic and mass transport effects. We do this using a series of approaches. First, we compare the polarization curves obtained for a series of different loadings of 'catalyst'. Since we do not know the total number of catalyst sites in the catalyst used, we simply refer to the loading of carbon powder containing the active sites formed during pyrolysis. We have also increased the number of data points obtained in the kinetic region of the polarization curve. This region is generally underdetermined in most polarization studies of fuel cells regardless of catalyst type, resulting in a lack of data points for fitting of kinetic parameters. We also use oxygen partial pressure as a variable to generate additional information about both kinetics and mass transport.

Results and discussion

Physicochemical characterization

TEM images of the CHF-1 catalyst pyrolyzed at 700 °C are presented in Fig. 2. These images show the presence of Fe particles distributed throughout the carbon structure (Fig. 2A). The average Fe particle size calculated from the images is 13 nm.

The presence of a shell of graphite can be observed (Fig. 2B), as has been reported previously with iron(III) tetramethoxyphenyl porphyrin chloride (FeTMPP-Cl) pyrolyzed at 1000 °C (ref. 44) and polyaniline derived electrocatalysts at 900 °C.[2] Particles surrounded by graphitic shell exhibit a higher resistance to dissolution in acidic medium and therefore higher stability in the fuel cell environment. The carbon structure observed by TEM imaging (Fig. 2C and D) is defined as turbostratic or mesographitic, given that the basal planes are not well-aligned compared to an ideal fully graphitized carbon structure.

SEM images of the as-synthesized (Fig. 3A and B), 700 °C pyrolyzed (Fig. 3C and D) and acid treated with a second 700 °C heat treatment (Fig. 3E and F) samples. The images A, C and E are the back-scattered electron (BSE) images. As expected, the as-synthesized material (Fig. 3A) does not exhibit metal particles formation, given that at this point the iron is embedded in the organic structure. However, in the heat treated samples

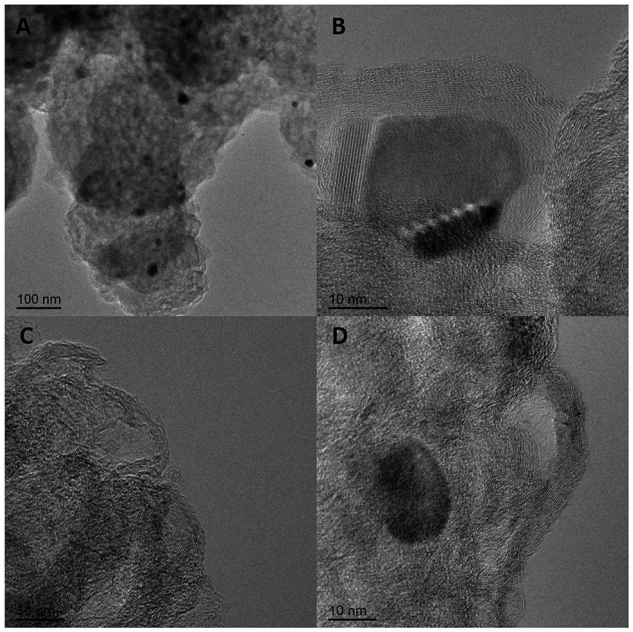

Fig. 2 High-resolution (HR) TEM images of the 700 °C pyrolyzed iron porphyrin framework based catalyst (A) HRTEM image of the iron nanoparticle distribution on the catalyst structure. (B) HRTEM image showing an onion-like mesographitic nanoshell surrounding Fe particle. (C) HRTEM image showing the mesographitic structure of the carbon support. (D) HRTEM image of a typical non-precious metal catalyst nanostructure involving carbon and metal aggregates.

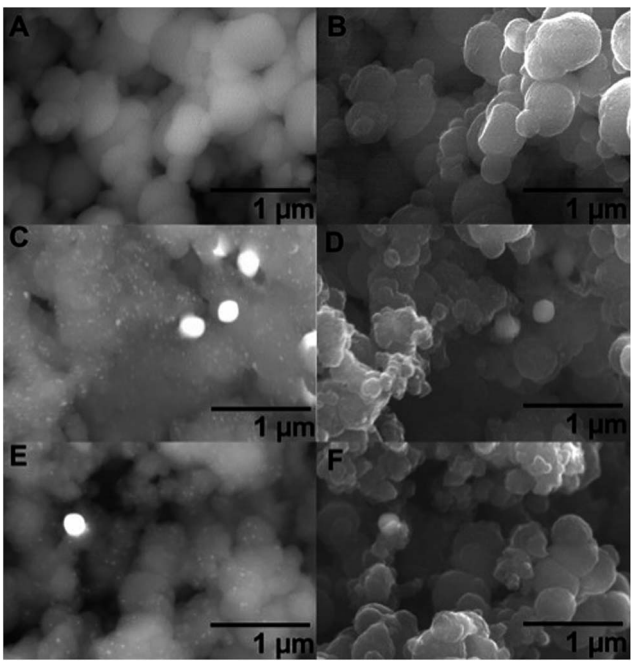

Fig. 3 Back-scattered and secondary electron images of the highly porous as-synthesized (A and B), 700 °C pyrolyzed (C and D) showing the presence of iron nanoparticles, and acid treated (E and F) CHF-1 catalyst. The latter exhibits a lower density of metal particles and a higher porosity (Table 2) as a result of the acid leaching process.

before (Fig. 3C) and after (Fig. 3E) acid treatment, the Fe particles formed during the pyrolysis process are easily visualized (due to its higher atomic number). The particles show a uniform distribution throughout the sample, with the presence of few agglomerates, both before and after acid treatment. In agreement with previous observations by Ma *et al.*,[41] the as-synthesized CHF-1 (Fig. 3A and B) structure is composed of agglomerated ball-shaped particles (200–400 nm diameter), exhibiting a high surface area and pore volume (0.442 $cm^3\ g^{-1}$), as confirmed through BET results (see Table 1). On the other hand, the samples after pyrolysis (Fig. 3C–F) exhibit more extensive agglomeration and a heterogeneous particle size distribution, which causes an evident decrease of the surface area and pore volume (Table 1). However, it is worth noting that the sample subjected to acid leaching (Fig. 3E and F), not only exhibits a lower density of metallic particles, but a better defined structure in terms of exposed area and porosity (Table 1).

The metal content was evaluated though ICP-OES and SEM-based energy dispersive X-ray spectroscopy (EDS) analysis (Table 2), showing a decrease of 50% in the Fe content after acid treatment. Differences in the composition measured with the two techniques can be related to the volume of material analyzed using the SEM-EDS technique, in comparison to ICP-OES, which is a bulk composition analysis technique.

The XRD patterns corresponding to the as-synthesized and pyrolyzed (before and after the acid treatment) samples are presented in Fig. 4. The presence of graphitic carbon ($2\theta = 26°$) and metallic Fe (110) ($2\theta = 45°$) can be appreciated in both pyrolyzed samples (before and after acid treatment), in agreement with the observations made from TEM and SEM images.

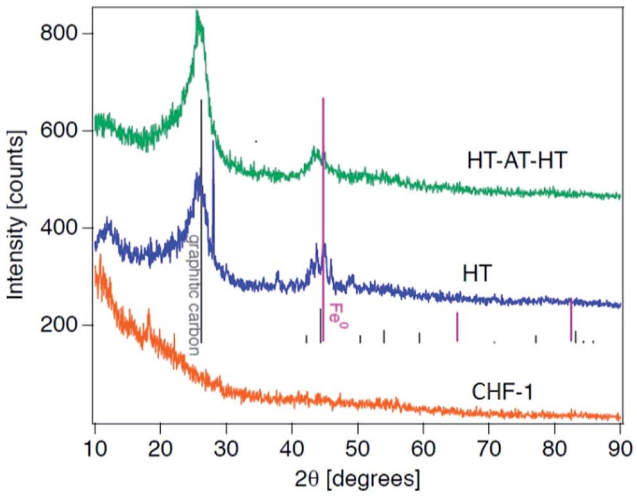

Fig. 4 Cu Kα X-ray diffraction patterns for the as-prepared catalyst (CHF-1), the catalyst after 700 °C heat treatment (HT), and the catalyst after 700 °C heat treatment followed by acid treatment and final 700 °C heat treatment (HT + AT + HT).

Catalytic activity: RRDE technique

Fig. 1 shows the RDE plots for the as-synthesized and pyrolyzed (before and after acid treatment) samples (A) and the number of electrons transferred measured using RRDE with a Pt ring (B). From Fig. 1A, it can be observed that the as-synthesized material does not show significant activity towards the ORR (−0.048 V onset potential). The samples subjected to heat treatment exhibit a significant improvement in catalytic activity with an onset potential of 0.868 V and 0.861 V (measured at the potential at which the current density reaches 50 μA cm^{-2}) for the samples before and after acid treatment, respectively. This increase in the onset potential (compared to the as-prepared sample) has been correlated with the graphite shell formation (Fig. 2B) in previous studies.[44] The acid-treated sample yielded a higher limiting current density. The higher current density could be explained by the removal of excess metallic particles that could potentially hinder the access of the reactants to the active sites (Table 2) or by the rearrangement of the catalyst structure through the second heat-treatment that can lead to the formation of new active sites.

The number of electrons transferred calculated through RRDE was 3.8 electrons in the limiting current region, as observed in Fig. 1B for the pyrolyzed samples (before and after acid treatment), which implies that the peroxide production is approximately 10% of the product. This result suggests that the reaction is mainly proceeding through the four-electron transfer path.

When the oxygen partial pressure is varied, the current density on the RDE plots changes as a function of the oxygen partial pressure. As an example, plots for 20, 40, 60, 80 and 100% oxygen are shown in Fig. 5. The inset plot shows the direct correlation between the oxygen partial pressure and the limiting current density.

Table 1 BET measurements of material

Material	BET surface area [$m^2\ g^{-1}$]	Pore volume [$cm^3\ g^{-1}$]
CHF-1 (Fe) (as-prepared)	1526.326	0.442
CHF-1 (700 °C)	288.883	0.100
CHF-1 (700 °C + AT + 700 °C)	393.389	0.129

Table 2 Fe content of material before and after heat/acid treatment measured with ICP-OES and EDS

Material	ICP-OES Fe content (%)	EDS Fe content (%)
CHF-1 (as-prepared)	5.64	11.82
CHF-1 (700 °C + AT + 700 °C)	3.84	5.73

Fuel cell testing

The iR_Ω-free polarization and resistance curves obtained from MEAs comprising iron porphyrin framework based cathodes with different catalyst loadings (1 $mg_{cat}\ cm^{-2}$, 2 $mg_{cat}\ cm^{-2}$ and 3 $mg_{cat}\ cm^{-2}$) are shown in Fig. 6. The current density, which is relatively low ($\leq 2 \times 10^{-5}$ A cm^{-2}) above 0.7 V, increases to

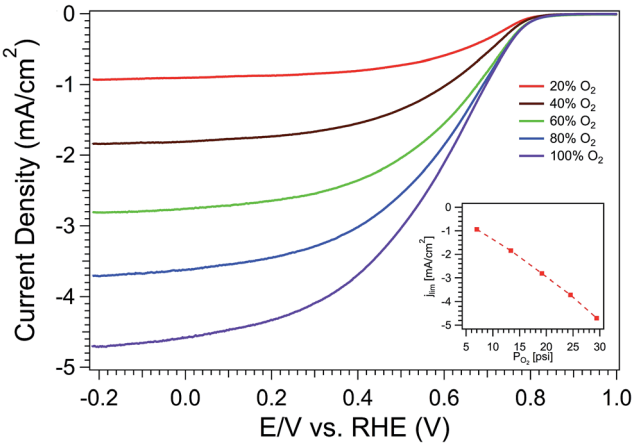

Fig. 5 RDE curves for the pre-treated iron porphyrin framework at different oxygen partial pressures. 1600 rpm, 10 mV s^{-1} scan rate. 0.1 M H_2SO_4 electrolyte, Hg/Hg_2SO_4 reference electrode and Au wire counter electrode.

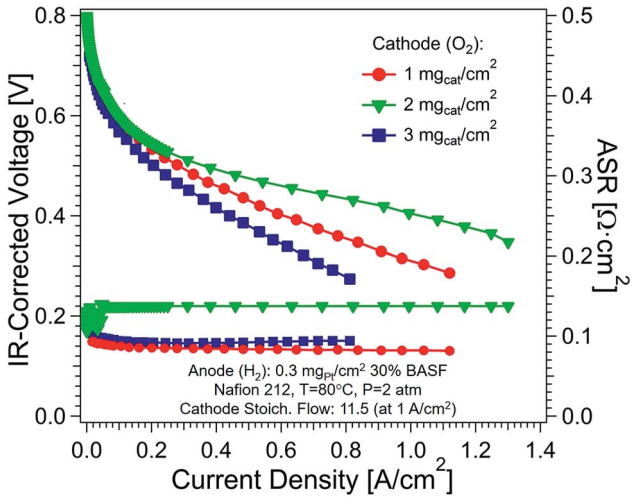

Fig. 6 Polarization and resistance curves for H_2–O_2 PEM fuel cells with different cathode catalyst loadings: 1 mg_{cat} cm^{-2} (●), 2 mg_{cat} cm^{-2} (▼) and 3 mg_{cat} cm^{-2} (■). The curves were obtained with inlet gases heated and humidified to 83 °C, 2 atm backpressure and the cell temperature was held at 80 °C.

ca. 0.10 A cm^{-2} at 0.6 V for all loadings. The maximum power density for 2 mg_{cat} cm^{-2} is 0.46 W cm^{-2}, for 1 mg_{cat} cm^{-2} catalyst loading is 0.32 W cm^{-2} compared with 0.22 W cm^{-2} for 3 mg_{cat} cm^{-2}, suggesting a significant influence of the CL loading on the performance of the PEMFC. A loading of 2 mg_{cat} cm^{-2} provided the best results in terms of FC performance. This data, obtained at 100% O_2, gives a first glimpse of the behavior of this system. The stability of this material is discussed in the ESI (Fig. S3†).

To provide data for a more extensive analysis, we probe the influence of oxygen partial pressure variations on the performance of the material, shown for the best performing loading (2 mg_{cat} cm^{-2}) in Fig. 7. This data is typical of all loadings. Significant decreases in current density obtained at a given cell

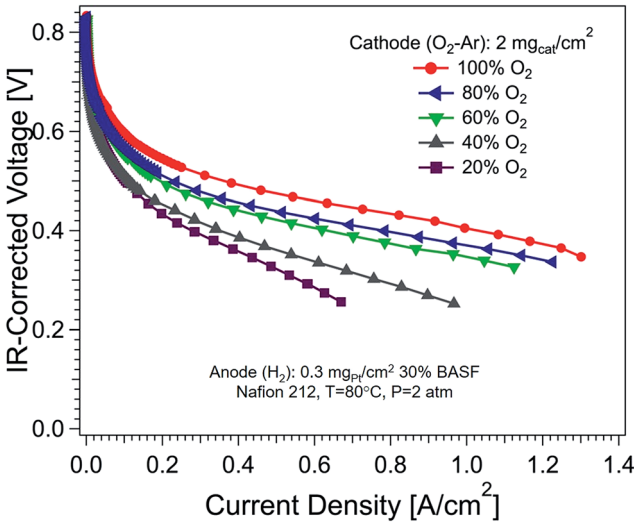

Fig. 7 Polarization curves for PEM fuel cells with 2 mg_{cat} cm^{-2} cathode catalyst loading and oxygen partial pressure variation: 20% O_2 (SF: 2.8), 40% O_2 (SF: 5.2), 60% O_2 (SF: 7.5), 80% O_2 (SF: 9.5) and 100% O_2 (SF: 11.5). The curves were obtained with inlet gases heated and humidified to 83 °C, 2 atm backpressure and the cell temperature was held at 80 °C (SF: cathode stoichiometric flow at 1 A cm^{-2}).

voltage are observed in most regions of the polarization curve. To further interpret these results, we must analyze both kinetics and mass transport aspects revealed by the data.

The iR_Ω-free polarization curves acquired with different catalyst loadings and oxygen partial pressure were analyzed using the Tafel equation (eqn (1)) at low current densities where mass-transfer effects can be neglected. Hydrogen crossover is assumed to assert minimal influence on the observed kinetics.

$$\eta_{act} = a + b\log(i) \quad (1)$$

where,

$$a = \frac{2.3RT}{\alpha F}\log(i_0) \text{ and } b = -\frac{2.3RT}{\alpha F} \quad (1a)$$

where η_{act} is the activation overpotential associated mainly with the sluggish O_2 reduction reaction kinetics, a and b are the Tafel parameters, i_0 is the exchange current, α is the cathodic transfer coefficient, R is the gas constant, F is the Faraday constant and T is the cell temperature.

Taking a and b as free parameters, least squares fitting was applied to find the best fits of eqn (4) to the polarization curves at the Tafel region (*i.e.* low current densities <0.1A cm^{-2}). The mass transport and proton conduction contributions in this region were found to be negligible based on an impedance analysis (Fig. S4–S7†) as well as by comparing mass transport j_{lim} to the current range over which the kinetic analysis was carried out. This is described in detail in the ESI.† A representative curve acquired with the best-performing loading and a 100% oxygen partial pressure is shown in Fig. 8A. In all cases, two regimes were observed. For low cell voltages ('Zone 1', $\eta > 0.45$ V *i.e.* $E_{cell} <$ 0.7 V), the average Tafel slope is high (118.0 ± 8.9 mV per decade), and at high cell voltages ('Zone 2', $\eta \leq 0.45$ *i.e.* $E_{cell} > 0.7$

V) the average Tafel slope is lower (53.6 ± 8.2 mV per decade). Table 3 contains the parameters obtained from the fits for all curves. Unlike the case of Pt or Pt alloy catalysts, in which two Tafel slopes are also observed, it is unlikely that the kinetics is affected by the formation of oxides or other surface reactions in different potential regimes. We speculate that the presence of these two well-defined regimes could be related to the interaction with two different types of catalytic active sites (perhaps Fe–N_4/C and Fe–N_2/C[43,45]). The presence of these two types of sites has been suggested in cases where an Fe and N precursor are simultaneously present in the pyrolysis process.[43,45] We also note that the two types of catalyst sites would then have radically different intrinsic rates based on expected values of i_0. At this point, we forgo a more detailed interpretation given the difficulties of exactly estimating this parameter for ORR *via* an unknown reaction. The parameters obtained at the low cell voltage range (Zone 1) were employed in the subsequent analysis.

Using these parameters to extrapolate the Tafel behavior over the entire current regime, we obtain an approximation of the 'kinetics-only' cell performance in the absence of both ohmic and mass transport overpotential (Fig. 8B). From the calculated polarization curves obtained for the different cathode catalyst loadings (Fig. 8B) a direct correlation is observed between the cathode catalyst loading and the resulting kinetic performance. This agrees with the expectation that a higher cathode catalyst loading would imply a higher quantity of available active sites for the reaction to take place. However, the real performance exhibits a different trend, indicating that the ohmic and mass transport contributions have a strong influence on the overall performance. In order to study these effects in more detail, the individual contributions of these effects were calculated.

Table 3 Tafel parameters obtained for PEM fuel cells with different catalyst loadings (1 mg_{cat} cm^{-2}, 2 mg_{cat} cm^{-2} and 3 mg_{cat} cm^{-2}) and oxygen partial pressure variation

Loading [mg cm^{-2}]	p_{O_2}	b_1 [mV dec^{-1}]	$i_{0,1} \times 10^4$ [mA]	b_2 [mV dec^{-1}]	$i_{0,2} \times 10^8$ [mA]
1	20%	−119.04	7.96	−67.96	95.07
	40%	−119.32	17.39	−62.32	60.59
	60%	−125.19	30.22	−65.97	147.66
	80%	−115.23	22.75	−50.22	3.21
	100%	−109.32	20.19	−50.39	5.13
2	20%	−123.15	42.23	−62.97	143.75
	40%	−121.96	32.09	−49.82	1.75
	60%	−127.47	92.56	−56.55	49.42
	80%	−129.79	190.44	−49.68	7.58
	100%	−126.06	88.85	−57.17	48.39
3	20%	−122.25	57.69	−52.39	18.48
	40%	−114.10	33.72	−44.29	0.76
	60%	−95.23	9.10	−42.50	0.72
	80%	−111.50	41.48	−44.30	1.46
	100%	−110.79	51.40	−47.59	12.80

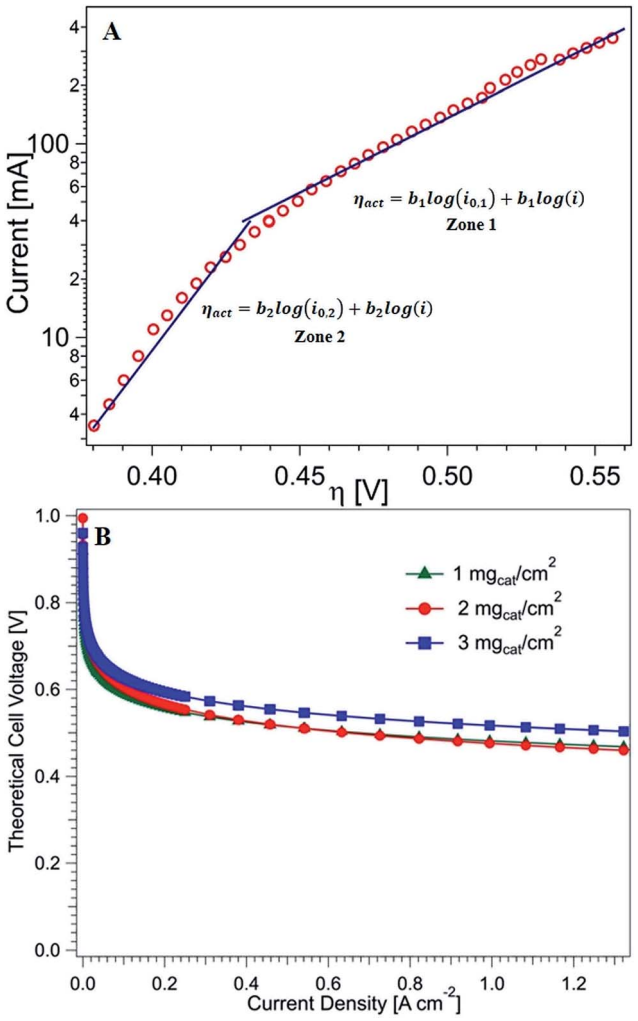

Fig. 8 (A) iR_Ω-corrected Tafel plot of an MEA with 2 mg_{cat} cm^{-2} PCPF-1 cathode and 0.2 mg_{Pt} cm^{-2} anode with a cathode feeding of 100% oxygen (markers) and fit to the Tafel equation (line) (B) theoretical polarization curves free of ohmic and mass transport losses.

To identify the individual voltage loss contributions, the cell voltage can be broken down in terms of the individual overpotential contributions:

$$E_{cell} = E_{rev}(p_{H_2}, p_{O_2}, 80\ ^\circ C) - \eta_{act} - \eta_{ohm} - \eta_{mt} \quad (2)$$

where E_{rev} is the reversible open circuit voltage, η_{ohm} is the overpotential due to ohmic losses caused by electronic contact resistances between the flow-fields and the diffusion media and ohmic resistance due to proton conduction through the membrane,[1] and η_{mt} is the concentration overpotential, associated to the transport of O_2 through the diffusion medium and the CL. As shown previously, η_{act} can be estimated through extrapolation of the Tafel equation. η_{ohm} was determined by multiplying the measured high-frequency resistance of the cell by the current density. *In situ* measured ohmic resistances for the different cells were approximately 0.25 ± 0.06 Ω cm^2, which is an order of magnitude higher than measurements for standard Pt supported on carbon cathode catalyst,[1] and can be related to a lower intrinsic conductivity of the cathode material. Higher metal content and degree of graphitization in the cathode material, along with improved membrane conductivity and contact resistances between flow-fields and diffusion

media, could contribute to the reduction of the overall voltage decline with increasing current density in the fuel cell performance for future designs.

The dashed line in Fig. 9A–C corresponds to the calculated polarization curves free of ohmic and mass transport losses for each cathode loading, shown previously in Fig. 8B. From these plots, we confirm that the activation overpotential accounts for the majority of the losses in the cell, as also shown in Table 4. η_{act} reaches values up to 759 mV (at 1.17 A cm^{-2} current density) with 1 mg_{cat} cm^{-2} cathode loading, which represents at least a 93% increase when compared to the values obtained at the same current density with a typical Pt supported on carbon cathode catalyst.[1]

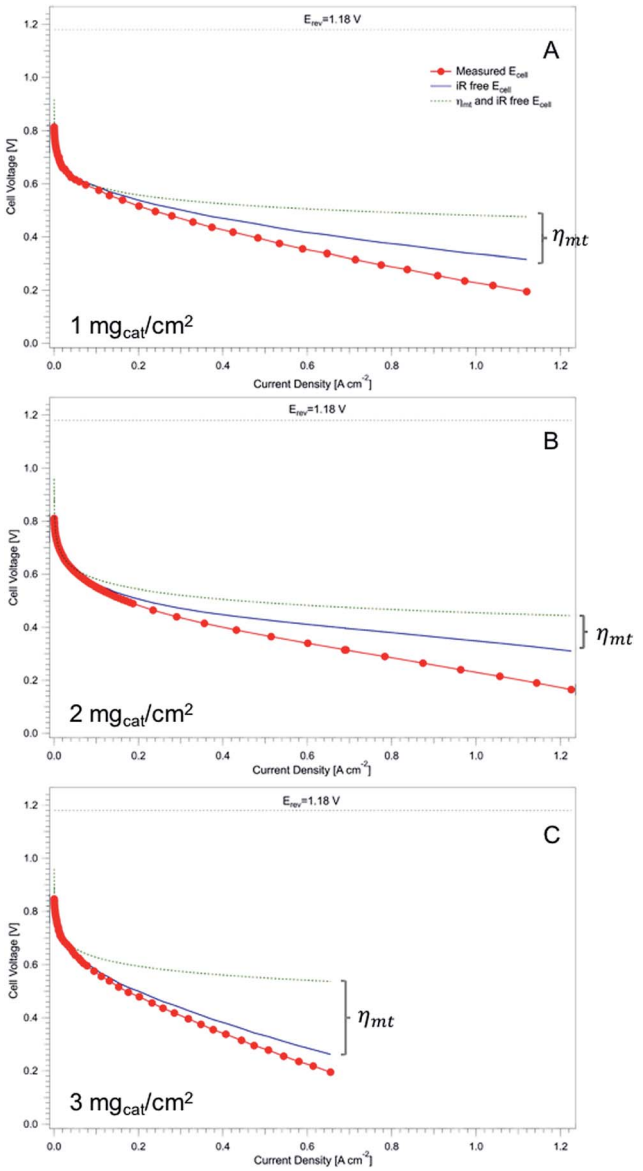

Fig. 9 Polarization curve for a PEM fuel cell with 1 mg_{cat} cm^{-2} (A), 2 mg_{cat} cm^{-2} (B), and 3 mg_{cat} cm^{-2} (C) cathode catalyst loadings. Each curve was obtained with inlet gases heated and humidified to 83 °C, 29.4 psia backpressure and the cell temperature was held at 80 °C. Calculated polarization curves are also included showing the effect of ohmic and mass transport overpotentials.

Table 4 Ohmic and mass transport voltage loss contributions at a fixed η_{act} and thickness for each cathode loading

Loading	Thickness [μm]	η_{act} [mV]	η_{ohm} [mV]	η_{mt} [mV]
1 mg_{cat} cm^{-2}	13.6	630.9	25.92	27.18
		92.2%	3.8%	4.0%
2 mg_{cat} cm^{-2}	46.6	630.4	21.26	33.4
		92.0%	3.1%	4.9%
3 mg_{cat} cm^{-2}	57.3	630.5	27.18	220.5
		71.8%	3.1%	25.1%

In Fig. 9, the solid line and the circle symbols represent, respectively, the mass-transport-voltage free cell voltage (result of the addition of the theoretical polarization curve and the measured ohmic losses) and the measured polarization curve. These polarization curves demonstrate the role of the ohmic and mass transport overpotentials on the overall performance of the fuel cell. In order to quantitatively appreciate this effect, the individual ohmic and mass transport contributions presented in Table 4 were calculated at fixed activation overpotential (η_{act} = 632 mV). From Table 4 it can be observed that the mass transport overpotential becomes more significant for a 3 mg_{cat} cm^{-2} cathode loading, playing a major role in bringing about the poorer performance obtained in comparison to the lower loadings. The measured thickness values for each loading are presented in Table 4, showing a direct correlation with the cathode catalyst loading.

In summary, through the analysis of the individual contributions to the voltage loss, a combined effect of both kinetic and mass transport contributions can be associated with the cathode loading influence on the cell performance shown in Fig. 6. Although the highest cathode loading (3 mg_{cat} cm^{-2}) studied implies a higher amount of active sites and, therefore, exhibits lower activation overpotential, this effect is counterbalanced by the significantly higher mass transport contribution (Table 4). This increase in the concentration overpotential could be related to larger mass transport limitations due to the thickness of the electrode. This effect might be reduced by increasing the active site density. In order to assess the effect of a higher density of active sites in the non-precious material, the performance of an 'ideal electrode' with reduced mass transport losses (η_{mt} obtained at 2 mg cm^{-2}) and ORR overpotential (η_{act} obtained at 3 mg cm^{-2}) was evaluated. The polarization and power curves for said material are presented in Fig. 10, along with those of the best-performing loading (2 mg_{cat} cm^{-2}). As shown in Fig. 10, an increase in the density of active sites improves the cell performance throughout the entire voltage range, increasing the maximum MEA power density to 0.65 W cm^{-2} (45% increment with respect to the best performing cathode loading).

Finally, we emphasize some aspects of our test methodology that we believe will be important as more reports of fuel cell tests of these catalysts are done in air, rather than the more common tests in oxygen. Of course, the former are the true practical test of the catalyst in a fuel cell. We suggest that it is important to effect a separation of kinetic and mass transport

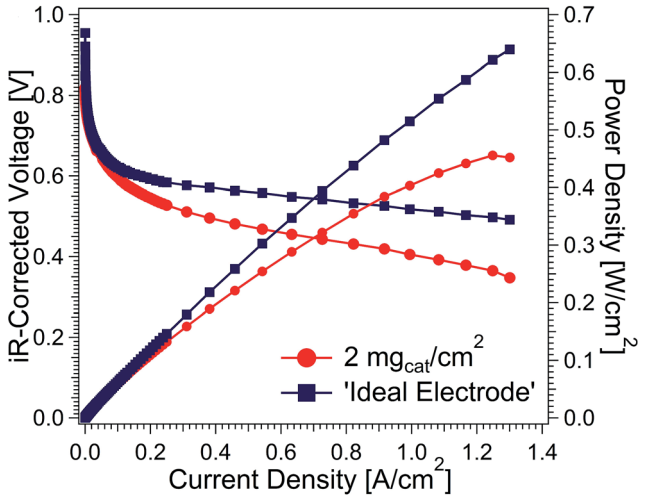

Fig. 10 Polarization and power curves for a PEM fuel cell with an ideal cathode result of the combination of the minimum overpotential losses and with 2 mg_{cat} cm^{-2} cathode catalyst loading (best-performing loading).

losses by testing in diluted oxygen streams as a first step in assessing the qualities of a catalyst and the electrode formed from that catalyst. In the absence of an accurate estimate of the number of active sites per unit amount of catalyst, this could allow us to probe indirectly the site density through comparing the onset point for significant mass transport effects, perhaps by analyzing Damköhler numbers.[46] Also, the inclusion of many more data points in the kinetic region of the polarization curve allows a more detailed kinetic analysis. Furthermore, each of these methods anticipates the requirements of modeling by providing more robust data sets that can be fit with greater statistical significance through simultaneous fitting of the family of curves as a function of oxygen partial pressure and through allowing the kinetics to be fit in a less cursory fashion than is typical. Indeed, our approach even lends itself to determining kinetic parameters outside the context of a given modeling framework, allowing a possible reduction in the number of adjustable fitting parameters for analysis of the entire polarization curve.

Conclusions

A pyrolyzed covalent heme framework was evaluated as a catalyst for the ORR. Pyrolysis followed by acid treatment was shown to be a determinant step towards the catalytic activity of this material. The H_2/O_2-Ar MEA performance was evaluated for different catalyst loadings and oxygen partial pressures to assess the mass transport influence on the performance of this material.

Through the analysis of the individual contributions to the voltage loss, a significant influence of the transport processes on the overall performance can be observed when the catalyst loading increases. A significant improvement of the overall cell performance was observed when the mass transport losses were 'artificially' reduced for the highest cathode catalyst loading.

Acknowledgements

Nelly M. Cantillo gratefully acknowledges the support from a Fulbright Fellowship. We gratefully acknowledge the support of this work by the NSF-funded TN-SCORE program, NSF EPS-1004083, under Thrust 2; funding from the US. Department of Energy Fuel Cell Technology program Grant #DE-EE0000459. Financial support from the National Science Foundation under Grant DMR-1352065 is also acknowledged (SM).

Notes and references

1 H. A. Gasteiger, S. S. Kocha, B. Sompalli and F. T. Wagner, *Appl. Catal., B*, 2005, **56**, 9–35.
2 G. Wu, K. L. More, C. M. Johnston and P. Zelenay, *Science*, 2011, **332**, 443–447.
3 H. T. Chung, C. M. Johnston, K. Artyushkova, M. Ferrandon, D. J. Myers and P. Zelenay, *Electrochem. Commun.*, 2010, **12**, 1792–1795.
4 U. I. Kramm, I. Herrmann-Geppert, P. Bogdanoff and S. Fiechter, *J. Phys. Chem. C*, 2011, 23417–23427.
5 S.-T. Chang, C.-H. Wang, H.-Y. Du, H.-C. Hsu, C.-M. Kang, C.-C. Chen, J. C. S. Wu, S.-C. Yen, W.-F. Huang, L.-C. Chen, M. C. Lin and K.-H. Chen, *Energy Environ. Sci.*, 2012, **5**, 5305–5314.
6 E. Proietti, F. Jaouen, M. Lefèvre, N. Larouche, J. Tian, J. Herranz and J.-P. Dodelet, *Nat. Commun.*, 2011, **2**, 416.
7 M. Lefèvre, E. Proietti, F. Jaouen and J.-P. Dodelet, *Science*, 2009, **324**, 71–74.
8 R. Jasinski, *Nature*, 1964, **201**, 1212–1213.
9 Y. Liu, X. Yue, K. Li, J. Qiao, D. P. Wilkinson and J. Zhang, *Coord. Chem. Rev.*, 2016, **315**, 153–177.
10 S. Gupta, D. Tryk, I. Bae, W. Aldred and E. Yeager, *J. Appl. Electrochem.*, 1989, **19**, 19–27.
11 G. Wu, Z. Chen, K. Artyushkova, F. H. Garzon and P. Zelenay, *ECS Trans.*, 2008, **16**, 159–170.
12 D. Ohms, S. Herzog, R. Franke, V. Neumann, K. Wiesener, S. Gamburcev, A. Kaisheva and I. Iliev, *J. Power Sources*, 1992, **38**, 327–334.
13 S. Ye and A. K. Vijh, *Electrochem. Commun.*, 2003, **5**, 272–275.
14 G. Liu, X. Li, P. Ganesan and B. N. Popov, *Appl. Catal., B*, 2009, **93**, 156–165.
15 A. Jindal, D. K. Gautam and S. Basu, *J. Electroanal. Chem.*, 2016, **775**, 198–204.
16 G. Lalande, R. Côté, D. Guay, J. P. Dodelet, L. T. Weng and P. Bertrand, *Electrochim. Acta*, 1997, **42**, 1379–1388.
17 C. Fabjan, G. Frithum and H. Hartl, *Berichte der Bunsengesellschaft für physikalische Chemie*, 1990, **94**, 937–941.
18 W. Seeliger and A. Hamnett, *Electrochim. Acta*, 1992, **37**, 763–765.
19 A. L. Bouwkamp-Wijnoltz, W. Visscher, J. A. R. van Veen and S. C. Tang, *Electrochim. Acta*, 1999, **45**, 379–386.
20 R. Bashyam and P. Zelenay, *Nature*, 2006, **443**, 63–66.
21 M. Yuasa, A. Yamaguchi, H. Itsuki and K. Tanaka, *Chem. Mater.*, 2005, 4278–4281.
22 W. Martínez Millán, T. Toledano Thompson, L. G. Arriaga and M. A. Smit, *Int. J. Hydrogen Energy*, 2009, **34**, 694–702.

23 W. Martínez Millán and M. A. Smit, *J. Appl. Polym. Sci.*, 2009, **112**, 2959–2967.
24 K. Lee, L. Zhang, H. Lui, R. Hui, Z. Shi and J. Zhang, *Electrochim. Acta*, 2009, **54**, 4704–4711.
25 T. E. Wood, Z. Tan, A. K. Schmoeckel, D. O'Neill and R. Atanasoski, *J. Power Sources*, 2008, **178**, 510–516.
26 G. Wu, K. Artyushkova, M. Ferrandon, A. J. Kropf, D. Myers and P. Zelenay, *ECS Trans.*, 2009, **25**, 1299–1311.
27 G. Wu, M. a. Nelson, N. H. Mack, S. Ma, P. Sekhar, F. H. Garzon and P. Zelenay, *Chem. Commun.*, 2010, **46**, 7489–7491.
28 P. Zamani, D. Higgins, F. Hassan, G. Jiang, J. Wu, S. Abureden and Z. Chen, *Electrochim. Acta*, 2014, **139**, 111–116.
29 P. Zamani, D. C. Higgins, F. M. Hassan, X. Fu, J.-Y. Choi, M. A. Hoque, G. Jiang and Z. Chen, *Nano Energy*, 2016, **26**, 267–275.
30 G. Goenaga, S. Ma, S. Yuan and D. Liu, *ECS Trans.*, 2010, **33**, 579–586.
31 S. Ma, G. A. Goenaga, A. V. Call and D.-J. Liu, *Chemistry*, 2011, **17**, 2063–2067.
32 A. Sarapuu, L. Samolberg, K. Kreek, M. Koel, L. Matisen and K. Tammeveski, *J. Electroanal. Chem.*, 2015, **746**, 9–17.
33 J. Anibal, H. G. Romero, N. D. Leonard, C. Gumeci, B. Halevi and S. Calabrese Barton, *Appl. Catal., B*, 2016, **198**, 32–37.
34 A. Morozan and F. Jaouen, *Energy Environ. Sci.*, 2012, **5**, 9269.
35 L. Yang, N. Larouche, R. Chenitz, G. Zhang, M. Lefèvre and J. P. Dodelet, *Electrochim. Acta*, 2015, **159**, 184–197.
36 F. Jaouen, J. Herranz, M. Lefèvre, J.-P. Dodelet, U. I. Kramm, I. Herrmann, P. Bogdanoff, J. Maruyama, T. Nagaoka, A. Garsuch, J. R. Dahn, T. Olson, S. Pylypenko, P. Atanassov and E. A. Ustinov, *ACS Appl. Mater. Interfaces*, 2009, **1**, 1623–1639.
37 H. J. Mackintosh, P. M. Budd and N. B. McKeown, *J. Mater. Chem.*, 2008, **18**, 573.
38 A. I. Cooper, *Adv. Mater.*, 2009, **21**, 1291–1295.
39 A. M. Shultz, O. K. Farha, J. T. Hupp and S. T. Nguyen, *Chem. Sci.*, 2011, **2**, 686.
40 Y. Zhang and S. N. Riduan, *Chem. Soc. Rev.*, 2012, **41**, 2083–2094.
41 X.-S. Wang, M. Chrzanowski, D. Yuan, B. S. Sweeting and S. Ma, *Chem. Mater.*, 2014, **26**, 1639–1644.
42 T. S. Olson, K. Chapman and P. Atanassov, *J. Power Sources*, 2008, **183**, 557–563.
43 *N4-macrocyclic metal complexes*, ed. J. Zagal, F. Bedioui and J. P. Dodelet, 2007.
44 S. L. Gojkovic, S. Gupta and R. F. Savinell, *J. Electrochem. Soc.*, 1998, **145**, 3493.
45 M. Lefèvre, J. P. Dodelet and P. Bertrand, *J. Phys. Chem. B*, 2002, **106**, 8705–8713.
46 E. L. Gyenge, *J. Power Sources*, 2005, **152**, 105–121.